



Numerical investigation of capacitive deionization (CDI) with divergent and convergent channels

Hooman Hadidi^{a,*}, Jafar Jamaati^b, Javad Ahmadi^c, Johan Nordstrand^d

^a Department of Mechanical Engineering, Kermanshah University of Technology, Kermanshah 6715685420, Iran

^b Department of Mechanical Engineering, Razi University, Kermanshah 6714414971, Iran

^c Department of Chemical Engineering, Amirkabir University of Technology (Tehran Polytechnic), Tehran 5748113478, Iran

^d Functional Materials, Applied Physics Department, School of Engineering Sciences, KTH Royal Institute of Technology, AlbaNova universitetscentrum, 106 91 Stockholm, Sweden

ARTICLE INFO

Keywords:

Capacitive deionization
Desalination
Modeling
Porous

ABSTRACT

This research aims to explore the impact of tilted channel configurations of CDI cells on desalination performance. The results reveal that the titled convergent channels have a faster average salt adsorption rate (ASAR) than the regular straight geometry. For desalination operations that end at a quarter of the equilibrium salt adsorption capacity (SAC), the convergent spacer with a slight slope of 1.5 degrees has a 20 % higher ASAR than the typical straight geometry (0.15 mg/g/min for convergent and 0.12 mg/g/min for straight). This gain increases to about 24, 29.5, and 33%, respectively, for slopes of 3.5, 5.5, and 7 degrees, compared to the straight geometry with the same spacer thickness. By looking at the underlying mechanisms, the spacer geometry is found to shift the location of the initial adsorption. This affects how quickly the device outputs the cleaned water. Interestingly, the geometry angle can also affect the location of the depletion zone, so tilted spacers can also affect the behavior during electrode starvation. Specifically, the convergent geometry has the depletion zone in the middle of the electrode instead of the corner near the outlet, as seen for straight and divergent channels. Together, these findings indicate how to construct tilted spacers to enhance CDI performance.

1. Introduction

In recent years, freshwater scarcity has become a global problem [1–6]. As a result, more attention has been paid to the improvement of sustainable and high-energy seawater desalination methods. One vital method to address the water crisis is desalinating the salty water. The capacitive deionization (CDI) method has been proven to be an efficient option for this purpose [3,4,6–13] and especially for brackish water desalination [14,15].

A CDI system polarizes the solution by using two electrodes through a potential difference. Adsorption of ions from solution to porous electrodes with opposite charges occurs [16–21]. The ions on the electrodes' surface are later released by removing or reversing the applied voltage. The main difference between CDI and supercapacitors is that there is fluid flow in the case of CDI, and the main goal is to desalinate rather than store the charges [22,23]. Previous studies have shown that carbons are the first choice for use in CDI because these materials have a relatively low cost and have shown good environmental compatibility [24–28].

Modeling has always been beneficial for researchers, and in the case of CDI, accurate modeling of the desalination mechanism in CDI cells is of great importance. Modeling makes predicting and optimizing system performance easier [29]. It has been reported that the previously used Gouy – Chapman – Stern (GCS) model does not have the accuracy required to simulate the CDI process [30]. Biesheuvel presented the modified Donnan (mD) model and showed that [31–35] modeling of salt absorption and charge storage in CDI systems under the effect of highly superimposed electric double layers is possible with this model. Guyes [35] employed a one-dimensional mD model and considered only charge and electric field transfer. In that work, a static feed solution between the electrodes was assumed, and the flow's impacts on ion absorption were not investigated. Numerous studies have tried to enhance the desalination efficiency of CDI cells by electrode material improvement [36–38] and parameter optimization [39–41].

Lee et al. [42], studying ion adsorption in NaCl solution, observed that ions are physically adsorbed to the electrodes' surface in a CDI system. This observation paved the way for further research in CDI cells.

* Corresponding author.

E-mail address: h.hadidi@shirazu.ac.ir (H. Hadidi).

Biesheuvel et al. [43] proposed a thermodynamic model to examine the charge efficiency of CDI. Their results showed an improvement in CDI charge efficiency due to an increase in battery voltage or a decrease in the solution's ionic strength. Dykstra et al. [44] showed that the Nernst-Planck equation could well model the CDI adsorption process. Recently, Nordstrand et al. [45] introduced the dynamic Langmuir (DL) model, which, while a simple model, can model the desalination process well. They extended the DL model two years later to a linear state-space model [46]. Using the mD model theory, Hemmatifar et al. [47] developed a two-dimensional (2D) CDI model that accounts for solution flows, charge transport, and electric field couplings. Although the proposed model considered the effects of the solution flow on the ion adsorption in the middle of the channel, it did not examine all effects of solution flow on the ion adsorption within the electrodes.

The impact of optimizing geometry on performance is more common in other applications than CDI. For example, convergent/divergent channels have been studied in applications relating to microchannels to achieve better mixing [48–55]. Implementing such changes in geometry and their impact on mixing can contribute to two significant effects. The first effect is to induce swirls that increase turbulence. The second effect is that the flows with different concentrations will have more time to mix when the residence time is increased in tilted geometries. Which of these effects is prominent depends on the Reynolds number. The application of such geometries has not yet been examined in CDI systems.

In the present study, it is shown how these geometries can affect the CDI systems by modeling fully coupled two-dimensional CDI in divergent and convergent geometries and comparing them with the straight channel. The deionization performance of the studied configurations has been compared and discussed in terms of cumulative salt adsorption, salt adsorption capacity (SAC), average salt adsorption rate (ASAR), and system dynamics. This research presents a theoretical framework for the optimal design of a practical desalination device.

2. Theory and numerical model

2.1. The two-dimensional modified Donnan model

To model the EDL structure and accumulation of the charge at porous electrodes, we apply the mD model [11,56]. The mD approach has a higher level of detail than a simpler EDL model, such as GCS [57]. The mD model is applied to bimodal pore structure electrodes in a formulation that describes the electrode double-layer formation [58]. In the model, porous electrode systems that have a volume with characteristic pore diameters smaller than or equal to the Debye length can be numerically treated [59], thus including overlapped Debye lengths. According to this model, macropores and micropores are distinguished. Further, ion transport is controlled by the volume occupied by the macropores, while the micropore volume controls the accumulating charge in the EDLs [35,58,60].

An electroneutral condition is assumed for ionic concentration in the macropores (i.e., no EDLs in macropore pathways). Additionally, micropore EDLs contain a compact Stern layer adjacent to the electrode surface. Micropore volume is regarded as strongly overlapped EDLs outside the Stern layer (In CDIs, Debye lengths typically are 1–10 nm [47]).

The coupled 2D adsorption-transport dynamics in a CDI cell were simulated using COMSOL Multiphysics 5.6. This software can simulate various problem models simultaneously, providing a powerful context for various physics [61–65].

Continuity and Navier–Stokes momentum conservation equations have the following form for the fluid flow in the main channel, respectively [66]. It should be noted that the spacer used in our models is not porous.

$$\nabla \cdot \mathbf{u} = 0 \quad (1)$$

$$\rho \left[\frac{\partial \mathbf{u}}{\partial t} + (\mathbf{u} \cdot \nabla) \mathbf{u} \right] = \mu (\nabla^2 \mathbf{u}) - \nabla P \quad (2)$$

where \mathbf{u} , P , μ , and ρ indicate the fluid velocity, pressure, viscosity, and density, respectively.

The porous media flow field is employed in the porous electrode region to obtain pressure and velocity distributions. In this zone, the fluid flow conforms to Darcy's law [67] by satisfying the continuous Stokes-Brinkman momentum conservation equation:

$$\frac{\rho}{p_M} \left[\frac{\partial \mathbf{u}}{\partial t} + (\mathbf{u} \cdot \nabla) \frac{\mathbf{u}}{p_M} \right] = \mu \frac{(\nabla^2 \mathbf{u})}{p_M} - \nabla P - \frac{\mu}{\kappa} \mathbf{u} \quad (3)$$

where p_M and κ represent the macropore porosity and effective permeability of porous media, respectively. In this model, $\kappa = 8.9 \times 10^{-12} \text{ m}^2$ and $p_M = 0.4$.

In the general form, ion transport can be described by the Nernst-Planck (NP) equation [68,69]:

$$\frac{\partial c_i}{\partial t} + \nabla \cdot \mathbf{J}_i = 0 \quad (4)$$

where c_i (unit mol/m³) denotes the concentration of species i , and the ion flux \mathbf{J}_i (unit mol/m².s) in the dilute solution can be expressed by:

$$\mathbf{J}_i = c_i \mathbf{u} - \frac{z_i D_i}{V_T} c_i \nabla \phi - D_i \nabla c_i \quad (5)$$

Here, D_i denotes the diffusion coefficient of the species in the spacer. ϕ indicates the local potential. The electrolyte is assumed to be dilute, binary, symmetric, and univalent ($z_i = 1$), with equal diffusion coefficients. Electroneutrality is maintained within macropores, and hence, $c = c_{M,i}$ for $i = \pm 1$.

Adsorption and desorption within electrodes are modeled by the following set of equations. For more detail about their derivations, the reader can refer to [47]. The electrochemical potential gradient between macropores and micropores disappears when the chemical equilibrium is reached. Hence, correlations between the ion concentration in micropores and macropores can be derived from an extended Boltzmann distribution [43].

$$c_{m,i} = c_{M,i} \exp \left(-z_i \frac{\Delta \phi_D}{V_T} + \bar{\mu}_{att} \right) \quad (6)$$

This equation encompasses $c_{m,i}$ and $c_{M,i}$ which are the concentrations of ion i in the micropores and macropores of the porous electrode, respectively; z_i represents the species valence; V_T denotes the thermal voltage ($V_T = KT/e$, where e denotes the charge of an electron. K and T are the Boltzmann constant and temperature, respectively; T is typically 293.15 K); $\Delta \phi_D$ represents the Donnan potential; and $\bar{\mu}_{att}$ from which the adsorption potential for ions into micropores can be calculated.

Micropore capacitance is related to the amount of charge stored in the micropores (the net amount) $2q_m$ (measured in moles per volume of the electrode) and the micropore potential drop $\Delta \phi_m$ (measured as the difference between the surface of the electrode and pore center) by using the formula below [47]. Here, C_m represents the effective volume-specific capacitance of micropores, while F denotes the Faraday constant.

$$2q_m F = -C_m \Delta \phi_m \quad (7)$$

Salt and charge balance in the porous media can be modeled using the following equations [47]:

$$\frac{\partial c}{\partial t} = D_e \nabla^2 c - \frac{p_m}{p - p_m} \frac{\partial w_m}{\partial t} \quad (8)$$

$$\nabla \cdot (c \nabla \phi) = \frac{p_m}{p - p_m} \frac{V_T}{D_e} \frac{\partial q_m}{\partial t} \quad (9)$$

Here, c represents the concentration of ions in macropores and bulk solution (i.e., $c = c_{M,i}$). Besides, $D_e = p_m D_i$ is defined as the effective diffusion coefficient in the porous media [64]. The volumetric ions concentration is represented by $2w_m = c_m^+ + c_m^-$, whereas the net charge density in micropores is expressed by $2q_m = c_m^+ - c_m^-$. The porosity of the micropores is denoted by p_m .

There is the following correlation among potentials of the solution ϕ , electrode ϕ_e , Donnan potential $\Delta\phi_D$, and micropore potential drop $\Delta\phi_m$ [47]:

$$\phi_e - \phi = \Delta\phi_m + \Delta\phi_D \quad (10)$$

It is noteworthy that ϕ_e varies with time. By non-dimensionalizing the above-mentioned equations, we get the following equations within the electrodes:

$$\frac{\partial \bar{c}}{\partial \bar{t}} = \bar{\nabla}^2 \bar{c} - \frac{p_m}{p - p_m} \frac{\partial \bar{w}_m}{\partial \bar{t}} \quad (11)$$

$$\bar{\nabla} \cdot (\bar{c} \bar{\nabla} \bar{\phi}) = \frac{p_m}{p - p_m} \frac{\partial \bar{q}_m}{\partial \bar{t}} \quad (12)$$

$$\bar{q}_m = -\bar{c} \exp(\bar{\mu}_{att}) \sinh(\Delta\bar{\phi}_D) \quad (13)$$

$$\bar{w}_m = -\bar{c} \exp(\bar{\mu}_{att}) \cosh(\Delta\bar{\phi}_D) \quad (14)$$

$$\bar{\phi}_e - \bar{\phi} = -\frac{2\bar{q}_m F}{C_m} + \Delta\bar{\phi}_D \quad (15)$$

In the spacer, the nondimensionalized equations will be as shown below. Notably, the transport equation in the spacer is based on the flux as mentioned in Eq. (8) and calculated based on the flow rate.

$$\bar{\nabla} \cdot (\bar{c} \bar{\nabla} \bar{\phi}) = 0 \quad (16)$$

In these equations, $\bar{t} = t L_e^2 / D_e$, $\bar{\phi} = V_T \bar{\phi}$, $\bar{c} = c_0 \bar{c}$, $\bar{q}_m = c_0 \bar{q}_m$, and $\bar{w}_m = c_0 \bar{w}_m$. L_e and L indicate the thickness and length of electrodes, respectively. Besides, c_0 shows the inlet concentration of the solution. In calculating the nondimensional effective micropore capacitance, \bar{C}_m , we use the formula $\bar{C}_m = C_m V_T / 2 F c_0$.

The calculation method of cumulative salt absorption during charging is represented here. Specific salt removal from the output stream at any given time can be obtained by the following equation [47]:

$$\Gamma_r(t) = \frac{1}{m_e} \int_0^t Q(c_0 - c_{out}(\tau)) d\tau \quad (17)$$

where m_e , $\langle c_{out} \rangle$ and Q indicate electrode mass, averaged effluent concentration over the outlet boundary, and flow rate of water, respectively

It is also possible to obtain specific adsorbed salt per electrode mass by the following expression. Here W is the depth ("into-the-paper" length) of the device. This value will be the same in all simulations, so the volume in different simulations will be the same if the 2D areas are the same.

$$\Gamma_a(t) = \frac{1}{m_e} \iint 2p_m(w_m(t) - w_m^0) W dx dy \quad (18)$$

Here, w_m^0 denotes the initial adsorbed charge at zero external voltage [47].

The following equation can do the calculation of the cumulative charge per electrodes mass:

$$\Sigma(t) = \frac{1}{m_e} \iint 2F p_m q_m(t) W dx dy \quad (19)$$

2.2. Geometry and boundary conditions

Three geometries have been studied: straight, divergent, and convergent channels. Two configurations have been evaluated with the slope (α) of divergent and convergent geometries equal to 1.5, 3.5, 5.5, and 7 degrees. In order to have comparable results, the spacer volume is considered the same among the three geometries in each configuration, equal to 6×10^{-6} , 9×10^{-6} , 1.5×10^{-5} , and 2×10^{-5} , respectively. Fig. 1 shows the schematic of the simulated CDI cells as straight, divergent, and convergent configurations. The electrodes are symmetric in all the configurations with an equal height (H_e), width (W), and length (L) of 0.68, 20, and 100 mm, respectively (i.e., the volume of $1.36 \times 10^{-6} \text{ m}^3$). There is a distance H_s between the electrodes to allow water to flow between them, equal to 3, 4.5, 7.5, 10, 15, and 20 mm in the straight channels of the cases with spacer volumes of 6×10^{-6} , 9×10^{-6} , 1.5×10^{-5} , 2×10^{-5} , 3×10^{-5} , and $4 \times 10^{-5} \text{ m}^3$, respectively. The inlet and outlet of length $L/8$ are included in the computation domain.

In this paper, all the geometries are shown in a scaled view to be visible in a compact figure. We have also represented cases with slopes of 10 and 12 degrees and spacer volumes of 3×10^{-5} and $4 \times 10^{-5} \text{ m}^3$ in the supporting information, which might be impractical to construct, made only for investigating the principles by looking at the extreme cases. However, in the following sections, the simulations show substantial gains even for small slopes, and having larger slopes improves the performance.

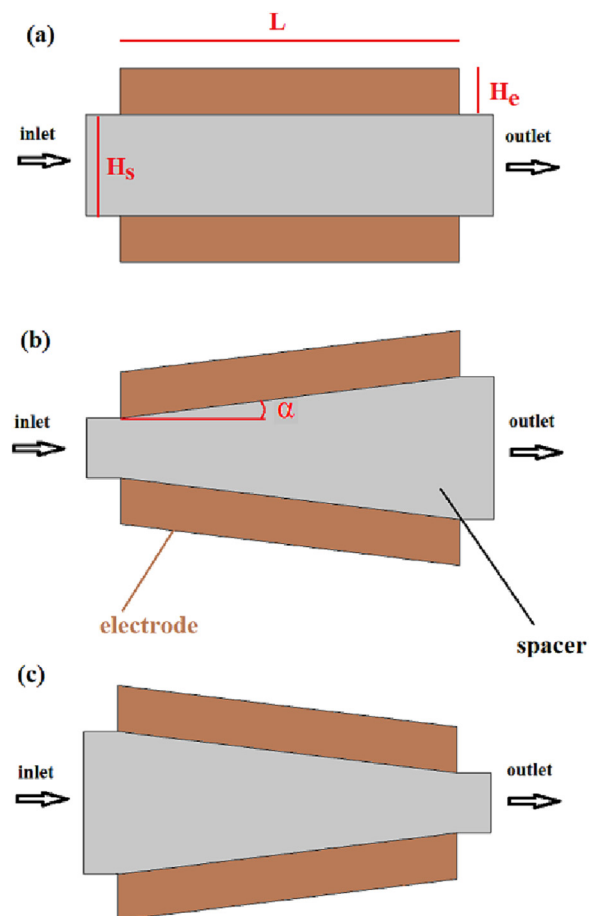


Fig. 1. Three geometries have been explored in this study: (a) straight, (b) divergent, and (c) convergent channels in various configurations of $\alpha = 1.5, 3.5, 5.5, 7, 10$, and 12 degrees. Convergent and divergent channels have the same spacer volumes as the straight geometry in each configuration.

Table 1

Values of the parameters in the mD model applied in our simulations.

parameter	description	value
p_m	The porosity of the micropores	0.3
p_M	The porosity of the macropores	0.4
R_c	Contact resistance	4.7Ω
C_m	The capacitance of the micropores	150 MFm^{-3}
D	The diffusion coefficient in the spacer	$1.9 \times 10^{-9} \text{ m}^2 \text{ s}^{-1}$
D_e	The effective diffusion coefficient in the porous media	$0.95 \times 10^{-9} \text{ m}^2 \text{ s}^{-1}$
μ_{att}	Parameter of the non-electrostatic salt adsorption	1.5

In all the investigated cases, an inlet constant flow rate of KCl with 20 mM concentration is implemented on the left side of the geometries. At the outlet, pressure has been set to zero on the right side of the channel. Besides, concentration has the value of $c = c_0$ at the inlet, or in a non-dimensional form, it is $\bar{c} = 1$. On the outer walls, we have $\partial \bar{c} / \partial n = 0$ and $\partial \phi / \partial n = 0$, in which \mathbf{n} is the normal vector at the walls. In other words, there is no flux through the outer walls (More details of the boundary conditions can be found in Fig. 1 (b) in Ref. [47]). In addition, the mass flux and current are constant at the boundary between the electrodes and the spacer, as explained in the previous work by Nordstrand and Dutta [64]. The macropore and micropore porosities of the activated carbon electrode are considered as 0.4 and 0.3, respectively. The model uses the parameters from Ref. [47] to make it comparable with earlier work in the literature. Table 1. provides a list of the parameters utilized in our study.

2.3. Grid independence study

The grid independence study was performed at the beginning of this research to ensure that the solution does not depend on the grids. The grid analysis of the geometries of the case with the slope of divergent and convergent geometries equal to 1.5 degrees is illustrated in Fig. 2 by plotting the variations in the adsorption for four different grid numbers. In all cases, there is a 0.8 V potential difference between the two electrodes; the inlet concentration equals 20 mol/m^3 , and the flow rate is 0.42 mL/min . As can be seen, for the straight geometry (Fig. 2b), the variations of the specific cumulative adsorption with grid number are minimal, and an acceptable result can be achieved with a relatively small number of meshes. For this reason, grid number 51,978 was chosen for this geometry for the rest of the calculations. The results show that the mesh affects especially the divergent (Fig. 2a) and convergent geometries (Fig. 2c). Therefore, grid numbers 682,317 and 705,814 have been used for these geometries, respectively. These selected grids show a negligible difference with a finer mesh. Close views of the grids used in the straight and divergent channels are given in Fig. S1. As a result of using boundary layers at the electrodes-spacer interface, the slopes of the convergent/divergent channels produced highly skewed elements that affected the results. Additionally, divergent/convergent channels have sharp corners at their inlet and outlet of the spacer, requiring much finer meshing. The grid independency condition was therefore met by significantly more grids in divergent and convergent models.

Another thing to note is that grid performance can vary depending on the type of calculation performed. Therefore, we repeated the dif-

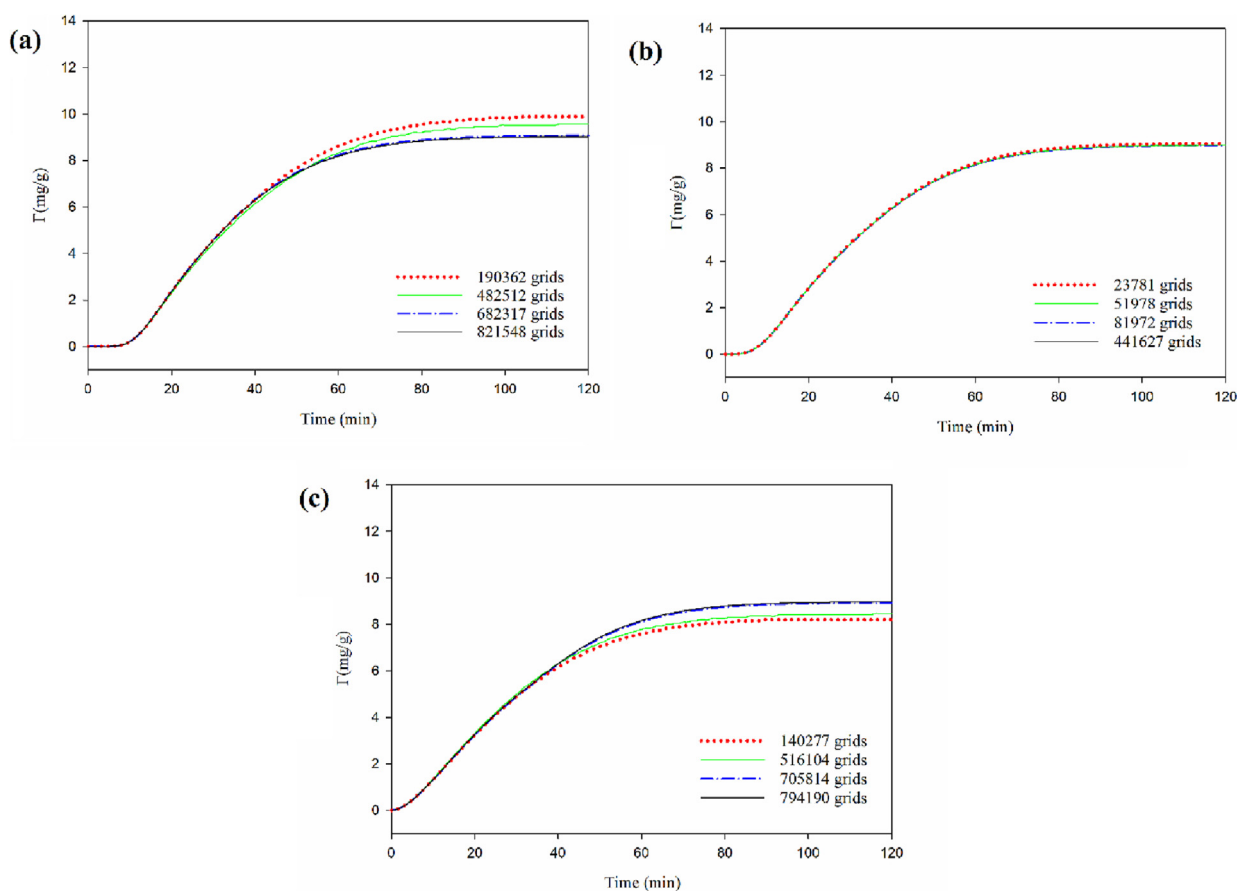


Fig. 2. Comparison of the adsorption evolution over time in (a) divergent, (b) straight, and (c) convergent geometries of the case with the slope of divergent and convergent geometries equal to 1.5 degrees.

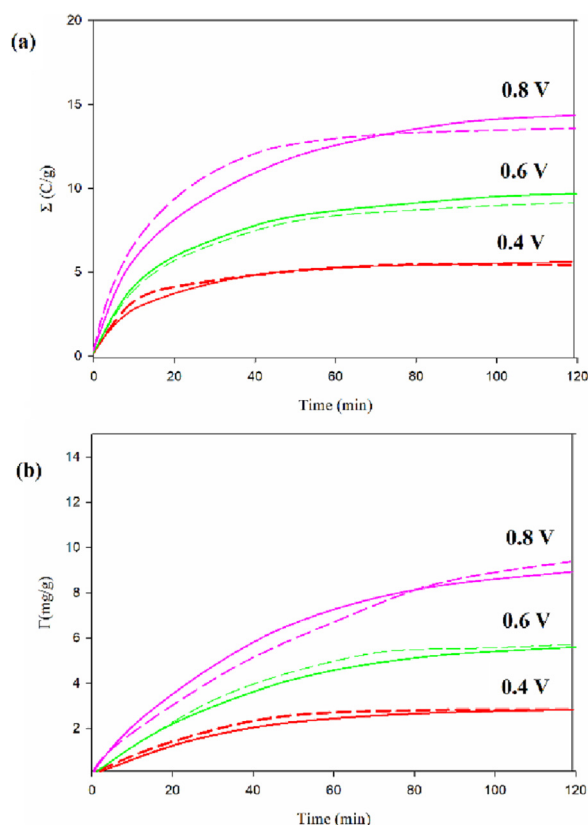


Fig. 3. Comparison of the (a) specific charge accumulation and (b) specific cumulative ion adsorption between our simulation results and those of experimental reports by Hemmatifar et al. [47] for three different applied voltages, 0.4 V, 0.6 V, and 0.8 V. The solid and dashed lines indicate the experimental and numerical results, respectively. The plots are reproduced from the previous work [64] using the same model.

ferent simulations with varying mesh sizes to verify the internal consistency of the results.

3. Results and discussion

In this section, the performance of the CDI system is examined for straight, divergent, and convergent channels. Before going into the main investigations, we first compare our results with previous experimental results to validate our numerical solution method.

3.1. Validation

In order to validate the model, the simulated cumulative charge and salt adsorption performance were compared with published experimental results for different applied voltages. As convergent/divergent spacers will be investigated theoretically in the study, it is necessary to ensure the model accurately describes CDI performance for a given geometry. Fig. 3 illustrates cumulative specific charge and salt adsorption variations over time for the same geometry as the experimental investigation of Hemmatifar et al.'s work [47]. Three potential differences of 0.4, 0.6, and 0.8 V are applied between the two electrodes. The concentration of the inflow is 20 mol/m^3 , and the mass flow is 0.42 mL/min in all investigated cases. As can be seen, there is a good agreement between our results and experiments [47], so the model appears to work well in a given geometry. Further validation of our simulation can be found in Ref. [64]. A validated model lets us make changes to the device structure and see how they affect the entire process.

The modeling results are the most accurate at low voltage. The biggest difference can be seen in the early charging process for 0.8 V. Here, the model overpredicts the cumulative charge somewhat. Earlier studies have reported that simulations of starvation conditions can be unsteady, so it is reasonable that this range should be more difficult to model accurately. The charging under normal conditions is mostly on an RC timescale, but the resistive losses in the solution matter more at low concentrations. This suggests that starvation conditions are more challenging to model accurately in this framework. However, the overall fitting is highly accurate.

3.2. Comparison of the CDI process dynamics among different geometries

This section evaluates CDI process dynamics by comparing the effluent concentration plot among the three geometries studied. Fig. 4 depicts variations of the normalized effluent concentration for the case with the slope of divergent and convergent geometries equal to 1.5, 3.5, 5.5, and 7 degrees. In all cases, the inlet flow rate and concentration are 0.42 mL/min and 20 mol/m^3 , respectively. The applied potential difference between the electrodes is 0.4 V and 0.8 V, respectively. For all geometries, the ion concentration at the output decreases rapidly to a minimum in a short time during the desalination phase. Then it gradually increases until the concentration of ions in the solution is approximately equal to the initial concentration of the solution. During this time, the activated carbon electrodes have reached saturation absorption capacity.

An interesting point from this figure is that the convergent geometry has faster kinetics in the time before reaching the minimum outlet concentration. It looks to reach this minimum point in around half the time of the normal spacer. On the other hand, the lowest effluent concentration is lower with the divergent geometry. The next section will go deeper into the quantitative performance differences between these geometries.

3.3. CDI system performance for straight, divergent, and convergent geometries

This section goes into more detail about the speed differences indicated in the last section. Here, we present results for cumulative specific salt removal for the straight, divergent, and convergent cell configurations. This corresponds to how much of the cleaned water has been pushed out of the CDI device. The slopes of the examined divergent and convergent geometries are equal to 1.5, 3.5, 5.5, and 7 degrees. The concentration of the inflow is 20 mol/m^3 , and the flow rate is 0.42 mL/min in all investigated cases. The applied potential difference between the electrodes is 0.8 V. As shown in Fig. 5(a), before reaching the equilibrium, the convergent geometry with a 1.5 degrees slope has higher cumulative salt adsorption than the straight channel. For example, the maximum difference is 0.75 mg/g after 10 mins of operation (0.57 for straight and 1.32 for convergent). On the other hand, for the divergent geometry with the same slope and time, we see about 0.36 mg/g lower cumulative salt adsorption compared to straight geometry. These differences in the performance diminish for longer operation times, and the geometries lead to the same adsorption at equilibrium. This suggests that convergent geometries could be beneficial to short operations.

Knowing that adding a slope can affect performance, we can look at Fig. 5(b–d), which displays the cumulative salt adsorption for steeper divergent and convergent geometries. For the cases with 3.5 and 5.5 degrees, the maximum difference of the cumulative salt adsorption between convergent and straight channels increases to 0.96 and 1.44 mg/g , respectively. For the 7 degrees configuration, the early cumulative adsorption has increased further in the convergent configuration. The operation with the convergent geometry removes 75.56% more than the straight geometry after 25 min (0.54 mg/g for straight and 2.21 mg/g for convergent). Fig. S2 depicts the results

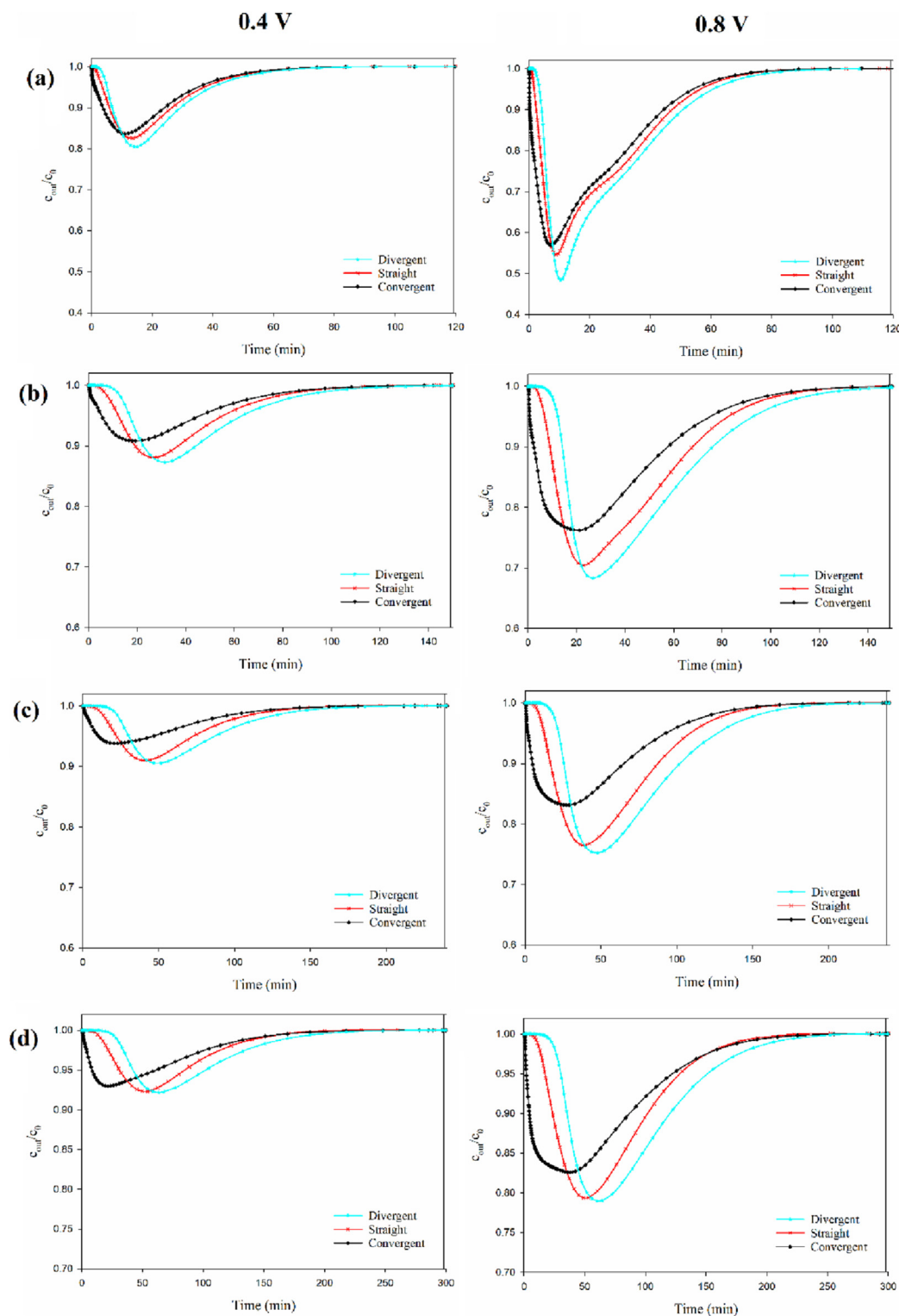


Fig. 4. Time evolution of the normalized effluent concentration for the case with the slope of divergent and convergent geometries equal to (a) 1.5 (b) 3.5 (c) 5.5 and (d) 7 degrees. The applied potential difference between the electrodes is 0.4 V (left) and 0.8 V (right).

for the cases with 10 and 12 degrees slopes. There are pronounced increases in early cumulative adsorption of the convergent channels, which demonstrates the importance of slope.

The difference matters because real CDI operations typically switch from desalination to regeneration well before equilibrium. Using the average salt adsorption rate (ASAR) as a performance indicator, we can measure how fast salt can be adsorbed, which is the salt amount

absorbed per cycle and divided by the cycle time [56]. The ASAR measures salt adsorption rate, or 'speed' [70]. To illustrate, for example, the equilibrium salt adsorption capacity (SAC) for all of the geometries of volume spacer $3 \times 10^{-6} \text{ m}^3$ in Fig. 5(a) is around 9 mg/g. However, the ASAR would be higher if the process was stopped earlier (see Fig. 6 (a)). For instance, with the straight channel, stopping at 2.25 mg/g (a quarter of equilibrium SAC) after 17 mins would yield an ASAR of

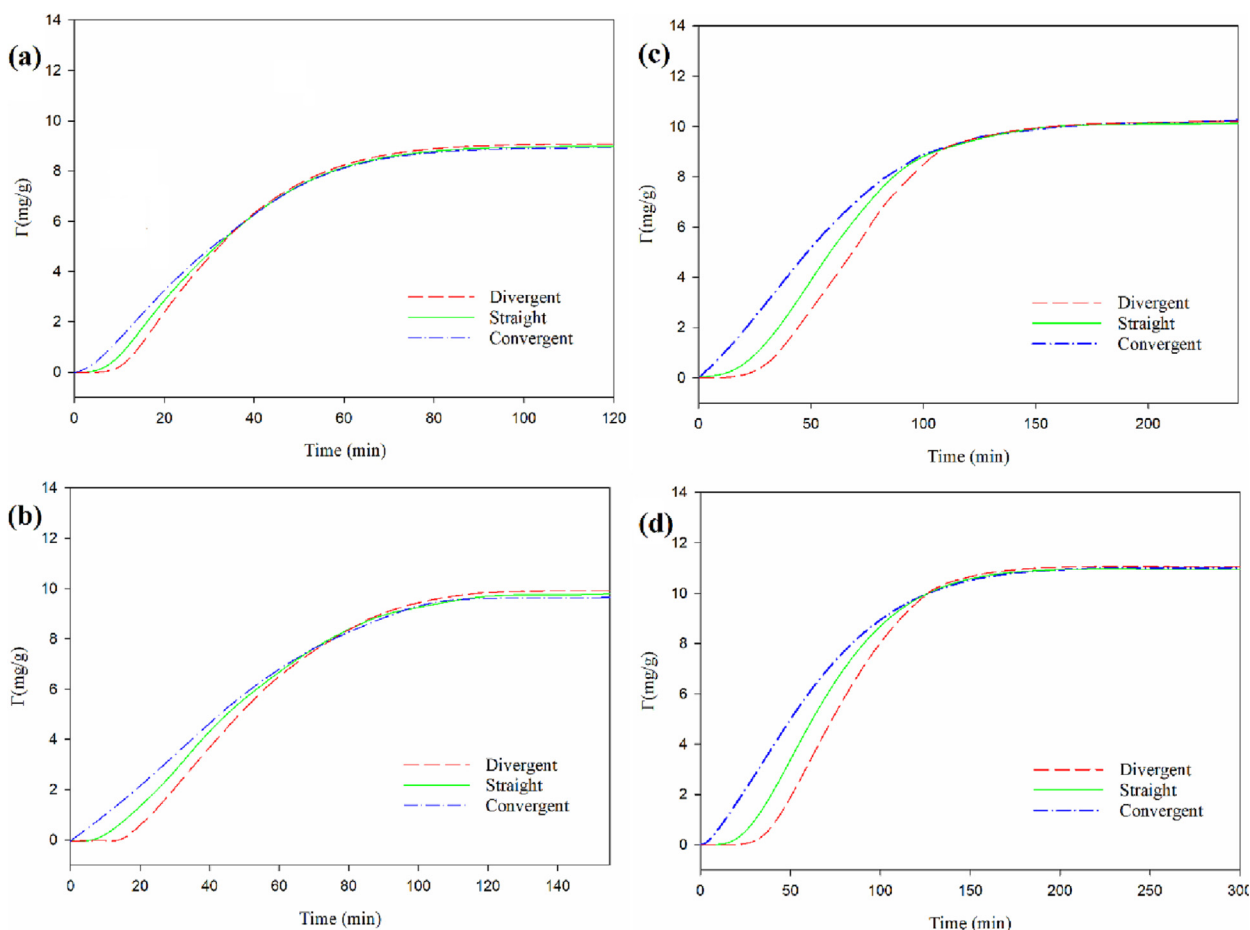


Fig. 5. Comparison of the cumulative specific ion adsorption evolution over time among three studied geometries with the slope of divergent and convergent geometries equal to (a) 1.5 (b) 3.5 (c) 5.5 and (d) 7 degrees.

0.12 mg/g/min instead of 0.07 mg/g/min for the equilibrium process after 120 mins (as shown in Fig. 6(a)). Meanwhile, stopping at a quarter of equilibrium SAC (at 15 mins) with the convergent geometry of 1.5 degrees improves the ASAR (0.15 mg/g/min) by 20 % compared to the same situation with the straight spacer.

For the geometries with slopes of 3.5, 5.5, and 7 degrees the gain improves to about 24, 29.5, and 33%, respectively. By examining the 7 degrees channel in more detail, it can be seen that the straight channel, stopping at 2.75 mg/g (a quarter of equilibrium SAC) after 45 mins, would yield an ASAR of 0.06 mg/g/min instead of 0.03 mg/g/min at the equilibrium state (as shown in Fig. 6(b)). While stopping at a quarter of equilibrium SAC with the convergent geometry of 7 degrees gives the ASAR of 0.09 mg/g/min at 30 mins. As illustrated in Fig. S3, for the convergent channels with slopes of 10 and 12 degrees, the performance improvement increases further to about 44 % and 57 %, respectively. However, the spacer is thick to accommodate the 10 and 12-degree slopes, so it should be viewed as a hypothetical model to illustrate the trend. That is, there is a trend that convergent geometries give a faster response in the early desalination process. For the 12-degree case, the straight channel, stopping at 3.25 mg/g (a quarter of equilibrium SAC) after 88 mins, would yield an ASAR of 0.03 mg/g/min instead of 0.02 mg/g/min at the equilibrium.

Fig. S4 shows the cumulative salt adsorption for the geometries with 7 degrees slope with an applied potential difference of 0.4 V instead. As can be seen, changing the voltage does not significantly affect the difference between the values associated with convergent/divergent geometries and the straight ones. Interestingly, Fig. S5

shows that the current is almost the same with all geometries. These initial results would suggest that the main reason the geometries perform differently is that they affect how quickly cleaned water is pushed out of the device.

From these results, it can be concluded that the convergent channels with a slight slope can effectively improve CDI performance compared to the straight channel. Also, steeper slopes yield bigger differences. This adsorption improvement does not depend on the applied voltage. It remains to explain why the tilted spacers would make a difference in the CDI process.

3.4. Distribution of normalized ion concentration in the spacer and macropores within different geometries

The previous sections have established that the spacer can affect the device output. This subsection looks at what happens inside the device, which could give a better understanding of the internal mechanisms and explain the results. Specifically, the results display concentration fields in convergent/divergent geometries with a slope of 7 degrees at charge times of 4, 84, and 150 mins with an equal spacer volume, including comparisons with the straight case. In all cases, a potential difference of 0.8 V is implemented between the two electrodes. The concentration of KCl solution at the inlet is 20 mol/m³. The flow rate has been set to a constant value of 0.42 mL/min. The applied potential difference between the two electrodes is 0.8 V. It should be noted that in all studied cases the flow is laminar due to the low Reynolds number, as discussed in section S5 of the supporting information.

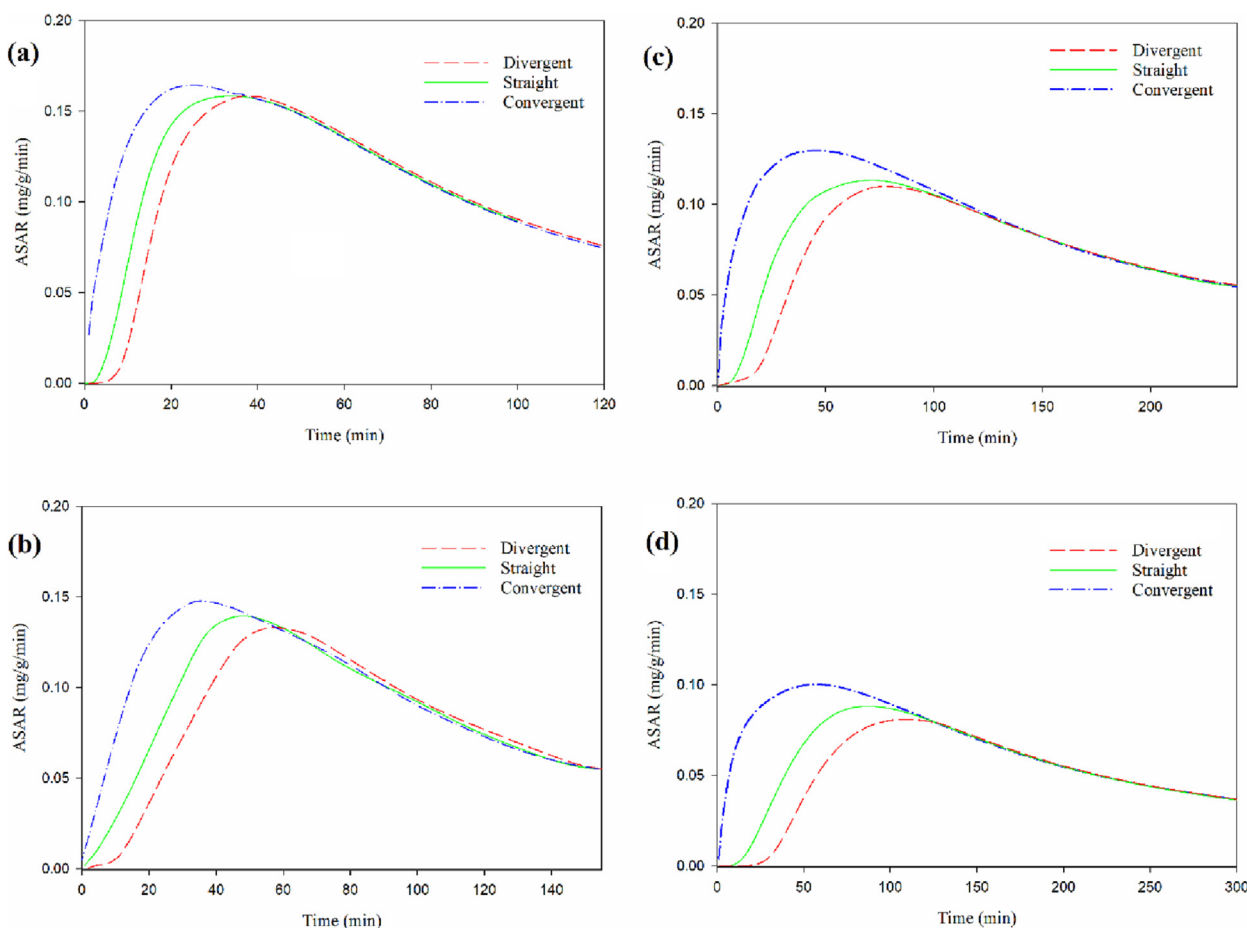


Fig. 6. Comparison of the average salt adsorption rate (ASAR) over time among three studied geometries with the slope of divergent and convergent geometries equal to (a) 1.5 (b) 3.5 (c) 5.5 and (d) 7 degrees. The applied potential difference between the electrodes is 0.8 V. Note that the reported ASAR is the cumulative value rather than the momentaneous removal rate. That is, the ASAR at a time t is calculated as the total removal up to t , divided by t .

In the cases of low initial concentration, after the external voltage ($t = 4$ min) is applied, a depletion zone close to the spacer at the electrode surface is formed due to the sudden absorption of ions from the macropores (Fig. 7). This starts at the electrode-spacer boundary. Interestingly, the depletion zone is first formed preferably at locations with a smaller spacer width in the simulations. We hypothesize that this is related to the lower electrolyte resistance in the spacer where the spacer is thinner. A key reason is that the high external resistance limits the overall current that can flow through the electrodes initially, but not the local ion current. This means the electrode could charge rapidly in some areas while charging slower in others. When multiple pathways are available through the spacer, the current takes the path of least resistance. Thus, the electrode areas closer to the thinner part of the spacer charge faster than the other electrode parts. Hence the location of the depletion zones.

At later times, this depletion zone grows, and its border extends to the top of the electrode to cover the entire electrode. Hemmatifar et al. [47] refer to this phenomenon as electrode starvation. It has been shown that in the low-concentration case, starvation can significantly retard the charging of the electrodes [47]. Interestingly, the location of the depletion zone at these later times can also be shifted by changing the geometry angle. The convergent geometry has the most uniform concentration, and its depletion zone is in the middle at $t = 84$ and 150 mins. Meanwhile, the straight geometry has depletion in the upper corner near the outlet.

One possible reason can be found in Eq. (8), which states that only diffusion affects ions transport in the electrodes. In all cases, the spacer channel near the outlet has a lower concentration than the inlet. Thus, the ions in the electrode around that area are replenished more slowly. This leads to more starvation. However, the convergent geometry removes ions near the outlet earlier in the charging process, giving more time for diffusion replenishment in that area and reducing the impact of starvation near the end of the charging process.

If the shift in the depletion zones mitigates starvation, that should be reflected in a higher current at intermediary times when the starvation raises the electrolyte resistance. The results show such behavior qualitatively (Fig. S6), although the effect is small. Thus, shifting of depletion zones seems to have a small impact on practical applications. Still, it gives an insight into the key mechanisms around tilted spacers. The following section will instead go deeper into the early adsorption patterns.

3.5. Distribution of normalized ion concentration in the electrode micropores within different geometries

The previous subsection hypothesized that the spacer angle shifts the position of the initial adsorption in the electrodes. Here, we will investigate that explicitly by looking at the adsorption (which is the same as the micropore concentration).

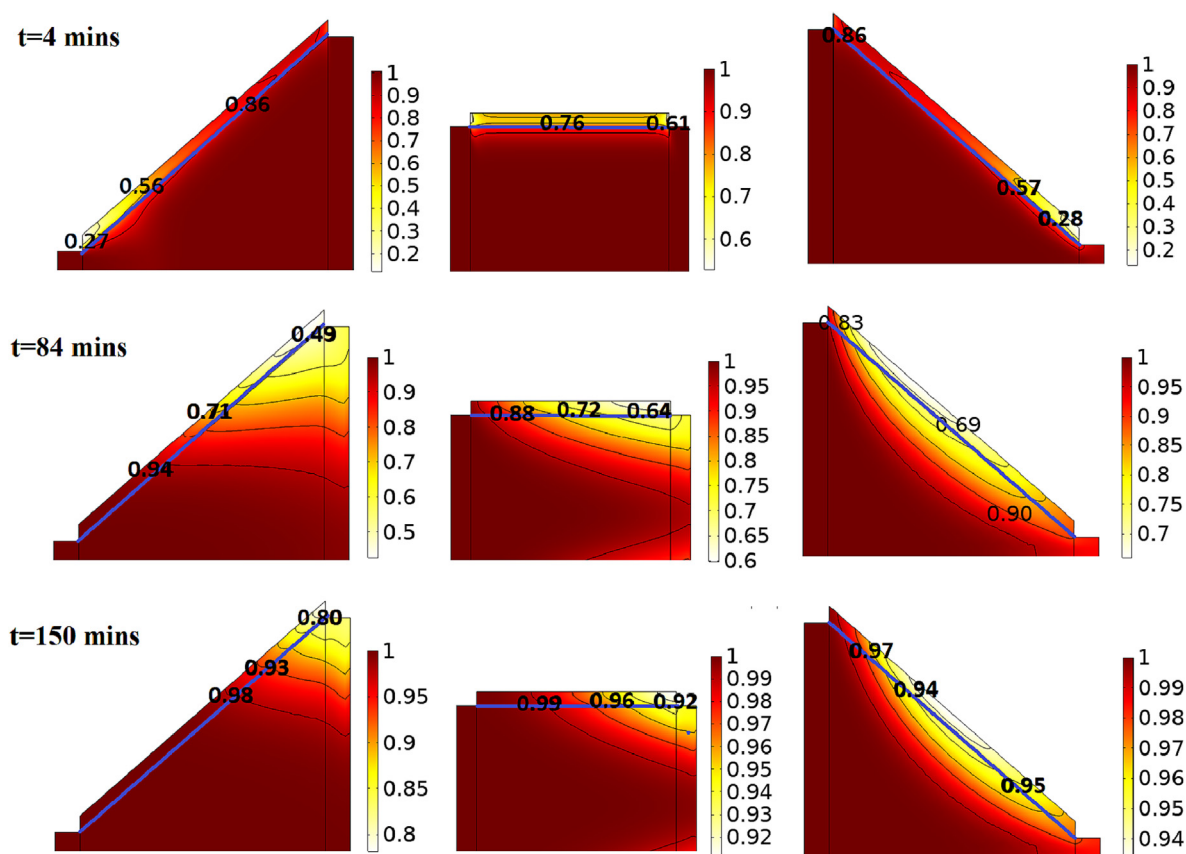


Fig. 7. The normalized concentration (c/c_0) distribution within the top half of the CDI cell at $t = 4, 84$, and 150 mins in the divergent (left) straight (middle) and convergent (right) geometries of the case with the slope of divergent and convergent geometries equal to 7 degrees. The electrode-spacer interface is indicated by a blue line.

An illustration of the charging process of the case with a slope of 7 degrees in the divergent/convergent channels is shown in Fig. 8. Specifically, the graphs focus on the normalized micropore adsorption within the upper electrode at times $4, 84$, and 150 mins. The results indicate that adsorption with the divergent spacer starts near the inlet and continues near the inlet. With a straight channel, the adsorption starts uniformly but continues near the inlet. An explanation would be that the influent water leads to a higher ion concentration near the inlet, which raises the diffusion rate and conductivity. So, it is natural to get higher adsorption there after a while. However, with a convergent spacer, the adsorption starts near the outlet before continuing near the inlet. This has a balancing effect on the overall adsorption distribution, particularly at the interface. That is, the early charging near the outlet seems to compensate for the inherent tendency to charge faster near the inlet. Hence the shift in depletion zones.

More importantly than depletion zones, the results demonstrate that the convergent spacers shift the initial adsorption towards the outlet (Fig. 8). This means there is a shorter way for the cleaned water to flow before exiting the device. That leads to faster output (Figs. 4–6). It also explains why the equilibrium results are the same in these figures because the spacer tilting only shifts where adsorption happens at what times. Conversely, the divergent spacer shifts adsorption towards the inlet. Thus, the water initially at the inlet would be cleaned more as it passes the spacer channel before it leaves the device. Thus, there will have been more total removal from the water when it finally exits, so the minimum effluent concentration is lower (Fig. 4).

3.6. Sensitivity analysis

Multiple steps have been taken to ensure that the simulation results are relevant to the experimental system. The core model was compared against experimental data with good agreement, meaning the local behavior on the electrodes is described accurately, and new geometries can be simulated with the same materials. Also, grid convergence studies were performed to ensure a high numerical precision under the varying geometries.

Four main slopes were considered. Already at a modest slope of 1.5 degrees, we can see a performance difference between the geometries. The larger slopes of $3.5, 5.5$, and 7 degrees (plus 10 and 12 in the Supplementary) are useful to clearly show the physical trends that come with larger slopes. Specifically, we have demonstrated faster output and shifting depletion zones compared to straight geometries with the same spacer thickness. The same trends exist for all slopes and become stronger for steeper slopes, which indicates that the simulated trends should be correct.

To practically accommodate the steeper slopes in the geometry, the spacer thickness was increased in these cases. So, Fig. 5(b–d) show a clear gain from using convergent spacers with $3.5, 5.5$, and 7 degrees compared to a straight spacer with the same thickness. However, the increased spacer thickness raises the resistance, meaning the gain in Fig. 5(b–d) is small compared to the situation in Fig. 3 with the thin straight spacer. Overall, we can thus say that a convergent spacer mainly improves performance if the average spacer thickness can remain small.

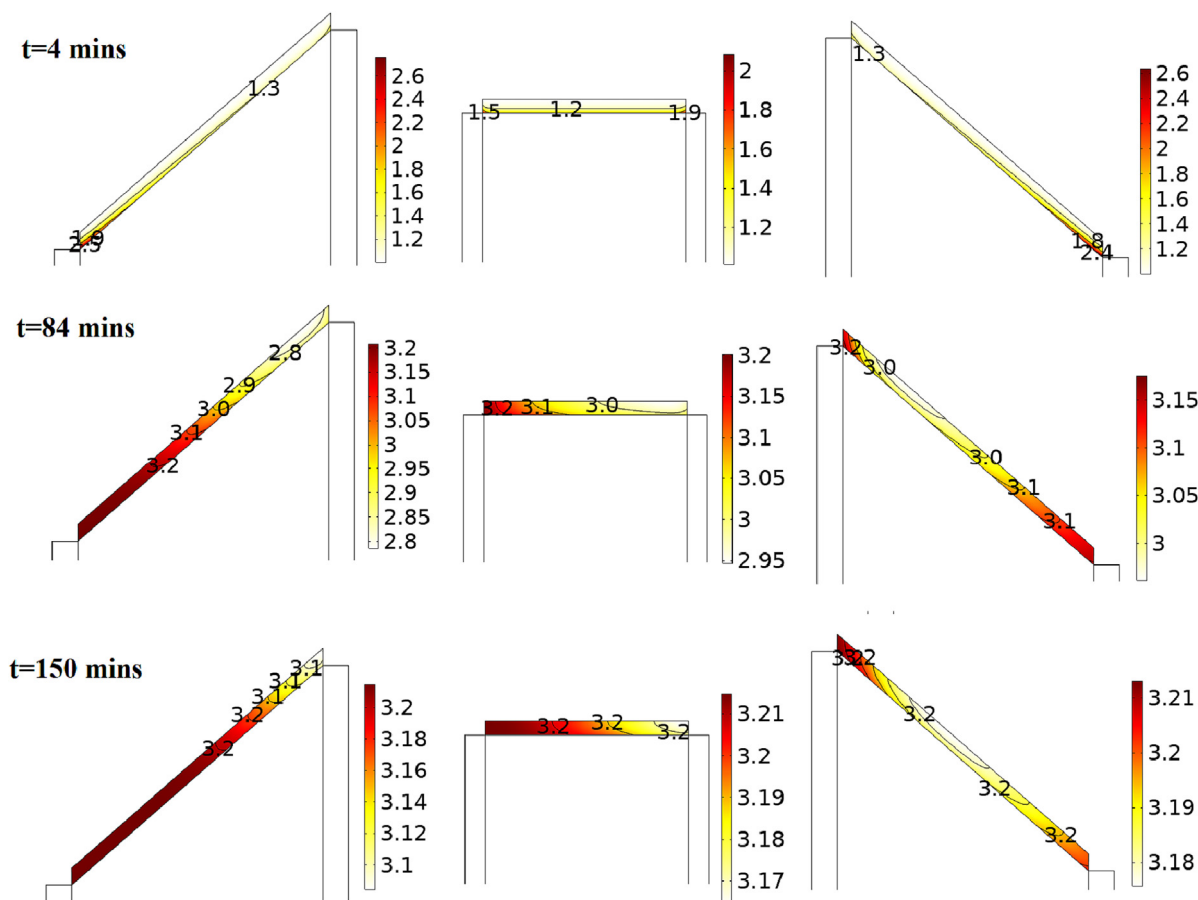


Fig. 8. Normalized micropore counterion concentrations within the upper electrode of the geometries in the case with a slope of 7 degrees in the divergent/convergent channels at times 4, 84, and 150 mins.

4. Conclusion

The present study attempts to gain a more comprehensive insight into CDI performance by modeling and comparing fully coupled two-dimensional CDIs in divergent and convergent geometries. These were compared to the straight channels with the same spacer and electrode volume. Our results show that the desalination output can be better in titled convergent channels than in straight ones with the same spacer thickness. For example, a convergent geometry of only 1.5 degrees improves ASAR by 20 % when stopping at a quarter of equilibrium SAC compared to straight spacers. This gain rises to about 24, 29.5, and 33%, respectively, for slopes as large as 3.5, 5.5, and 7 degrees, respectively. Also, the performance benefit is mainly tied to how quickly the cleaned water is pushed out of the device. Such results were almost the same regardless of the potential difference. Raising the spacer thickness to accommodate the sloped spacers can counteract the gains from the slope, so performance gains are seen mainly when there is a modest slope, and the spacer remains thin.

The study has provided several physical insights regarding how sloped spacers can affect the CDI process. These are related to the adsorption patterns and depletion zone formation within electrodes of the different geometries. As a trend, tilted spacers shift where the initial adsorption happens within the electrodes, which affects how quickly the clean water can be pushed out of the device. For example, convergent geometries shift the charging closer to the output, which yields a faster output response. Conversely, divergent geometries shift the initial charging towards the inlet, which leads to a lower minimal concentration in the output. Another trend is that the depletion zone location can be shifted by changing the angle of the channel. This

serves to mitigate concentration shocks, although the effect is small for practical purposes. Most uniform concentrations could be seen with convergent geometry. Instead of the corner near the outlet, as seen for straight and divergent channels, it has a depletion zone in the middle during the middle and late stages of the desalination process. All in all, tilted spacers give significant flexibility when tailoring the CDI operations for optimal performance.

CRediT authorship contribution statement

Hooman Hadidi: Conceptualization, Methodology, Software, Investigation, Writing – original draft. **Jafar Jamaati:** Conceptualization, Writing – original draft. **Javad Ahmadi:** Software. **Johan Nordstrand:** Validation.

Declaration of Competing Interest

The authors declare that they have no known competing financial interests or personal relationships that could have appeared to influence the work reported in this paper.

Acknowledgments

J.N would like to thank the Swedish research council (Diary No. 2018-05387) and J. Gust. Richert foundation (Diary No. 2020-00584) for funding the work.

Appendix A. Supplementary data

Supplementary data to this article can be found online at <https://doi.org/10.1016/j.jelechem.2023.117642>.

References

- [1] H. Kim, Y. Choi, S. Lee, K.-B. Lee, K.-W. Jung, J.-W. Choi, Pretreatment for capacitive deionization: feasibility tests using activated filter media and granule activated carbon filtration, *J. Ind. Eng. Chem.* 93 (2021) 253–258.
- [2] J. Gozalvez, J. Lora, J. Mendoza, M. Sancho, Modelling of a low-pressure reverse osmosis system with concentrate recirculation to obtain high recovery levels, *Desalination* 144 (1–3) (2002) 341–345.
- [3] Z. Ding, X. Xu, J. Li, Y. Li, K. Wang, T. Lu, M.S.A. Hossain, M.A. Amin, S. Zhang, L. Pan, Nanoarchitectonics from 2D to 3D: MXenes-derived nitrogen-doped 3D nanofibrous architecture for extraordinarily-fast capacitive deionization, *Chem. Eng. J.* 430 (2022) 133161.
- [4] Z. Chen, X. Xu, Y. Liu, J. Li, K. Wang, Z. Ding, F. Meng, T. Lu, L. Pan, Ultra-durable and highly-efficient hybrid capacitive deionization by MXene confined MoS₂ heterostructure, *Desalination* 528 (2022) 115616.
- [5] Y. Jande, W.-S. Kim, Predicting the lowest effluent concentration in capacitive deionization, *Sep. Purif. Technol.* 115 (2013) 224–230.
- [6] Y. Jande, W.-S. Kim, Modeling the capacitive deionization batch mode operation for desalination, *J. Ind. Eng. Chem.* 20 (5) (2014) 3356–3360.
- [7] H. Lim, Y. Ha, H.B. Jung, P.S. Jo, H. Yoon, D. Quyen, N. Cho, C.-Y. Yoo, Y. Cho, Energy storage and generation through desalination using flow-electrodes capacitive deionization, *J. Ind. Eng. Chem.* 81 (2020) 317–322.
- [8] P. Długolecki, A. van der Wal, Energy recovery in membrane capacitive deionization, *Environ. Sci. Tech.* 47 (9) (2013) 4904–4910.
- [9] J.-B. Lee, K.-K. Park, H.-M. Eum, C.-W. Lee, Desalination of a thermal power plant wastewater by membrane capacitive deionization, *Desalination* 196 (1–3) (2006) 125–134.
- [10] J.K. Lee, Y.E. Kim, J. Kim, S. Chung, D. Ji, J. Lee, Comparable mono and bipolar connection of capacitive deionization stack in NaCl treatment, *J. Ind. Eng. Chem.* 18 (2) (2012) 763–766.
- [11] M. Suss, S. Porada, X. Sun, P. Biesheuvel, J. Yoon, V. Presser, Water desalination via capacitive deionization: what is it and what can we expect from it?, *Energ. Environ. Sci.* 8 (8) (2015) 2296–2319.
- [12] Y. Li, Y. Liu, M. Wang, X. Xu, T. Lu, C.Q. Sun, L. Pan, Phosphorus-doped 3D carbon nanofiber aerogels derived from bacterial-cellulose for highly-efficient capacitive deionization, *Carbon* 130 (2018) 377–383.
- [13] Y. Gao, Z. Li, Z. Fu, H. Zhang, G. Wang, H. Zhou, Highly selective capacitive deionization of copper ions in FeS₂@ N, S co-doped carbon electrode from wastewater, *Sep. Purif. Technol.* 262 (2021) 118336.
- [14] S. Porada, R. Zhao, A. Van Der Wal, V. Presser, P. Biesheuvel, Review on the science and technology of water desalination by capacitive deionization, *Prog. Mater. Sci.* 58 (8) (2013) 1388–1442.
- [15] E.N. Guyes, A.N. Shocron, A. Simanovski, P. Biesheuvel, M.E. Suss, A one-dimensional model for water desalination by flow-through electrode capacitive deionization, *Desalination* 415 (2017) 8–13.
- [16] O.u. Haq, D.-S. Choi, J.-H. Choi, Y.-S. Lee, Carbon electrodes with ionic functional groups for enhanced capacitive deionization performance, *J. Ind. Eng. Chem.* 83 (2020) 136–144.
- [17] Q. Yao, H.L. Tang, Occurrence of re-adsorption in desorption cycles of capacitive deionization, *J. Ind. Eng. Chem.* 34 (2016) 180–185.
- [18] M.A. Anderson, A.L. Cudero, J. Palma, Capacitive deionization as an electrochemical means of saving energy and delivering clean water. Comparison to present desalination practices: will it compete?, *Electrochim. Acta* 55 (12) (2010) 3845–3856.
- [19] T. Welgemoed, C.F. Schutte, Capacitive deionization technology™: an alternative desalination solution, *Desalination* 183 (1–3) (2005) 327–340.
- [20] K. Wang, L. Chen, G. Zhu, X. Xu, L. Wan, T. Lu, L. Pan, Ferroferric oxide@ titanium carbide MXene heterostructure with enhanced sodium storage ability for efficient hybrid capacitive deionization, *Desalination* 522 (2022) 115420.
- [21] Y. Lester, E. Shaulsky, R. Epsztein, I. Zucker, Capacitive deionization for simultaneous removal of salt and uncharged organic contaminants from water, *Sep. Purif. Technol.* 237 (2020) 116388.
- [22] N. Shpigel, M.D. Levi, S. Sigalov, D. Aurbach, L. Daikhin, V. Presser, Novel in situ multiharmonic EQCM-D approach to characterize complex carbon pore architectures for capacitive deionization of brackish water, *J. Phys. Condens. Matter* 28 (11) (2016) 114001.
- [23] C. Hou, C. Huang, C. Hu, Application of capacitive deionization technology to the removal of sodium chloride from aqueous solutions, *Int. J. Environ. Sci. Technol.* 10 (4) (2013) 753–760.
- [24] G. Folaranmi, M. Bechelany, P. Sistat, M. Cretin, F. Zavisca, Comparative investigation of activated carbon electrode and a novel activated carbon/graphene oxide composite electrode for an enhanced capacitive deionization, *Materials* 13 (22) (2020) 5185.
- [25] K. Singh, S. Porada, H. de Gier, P. Biesheuvel, L. de Smet, Timeline on the application of intercalation materials in capacitive deionization, *Desalination* 455 (2019) 115–134.
- [26] S. Ntakirutimana, W. Tan, M.A. Anderson, Y. Wang, Editors' Choice—Review—Activated carbon electrode design: engineering tradeoff with respect to capacitive deionization performance, *J. Electrochem. Soc.* 167 (14) (2020) 143501.
- [27] G. Wang, B. Qian, Q. Dong, J. Yang, Z. Zhao, J. Qiu, Highly mesoporous activated carbon electrode for capacitive deionization, *Sep. Purif. Technol.* 103 (2013) 216–221.
- [28] F. Tabarkhooon, H. Abolghasemi, A. Rashidi, M. Bazmi, M.S. Alivand, F. Tabarkhooon, M.V. Farahani, M.D. Esrafil, Synthesis of novel and tunable Micro-Mesoporous carbon nitrides for Ultra-High CO₂ and H₂S capture, *Chem. Eng. J.* 456 (2023) 140973.
- [29] S. Porada, L. Borchardt, M. Oschatz, M. Bryjak, J. Atchison, K. Keesman, S. Kaskel, P. Biesheuvel, V. Presser, Direct prediction of the desalination performance of porous carbon electrodes for capacitive deionization, *Energ. Environ. Sci.* 6 (12) (2013) 3700–3712.
- [30] R. Zhao, P. Biesheuvel, H. Miedema, H. Bruning, A. Van der Wal, Charge efficiency: a functional tool to probe the double-layer structure inside of porous electrodes and application in the modeling of capacitive deionization, *J. Phys. Chem. Lett.* 1 (1) (2010) 205–210.
- [31] K. Kamran, M. Van Soestbergen, L. Pel, Electrokinetic salt removal from porous building materials using ion exchange membranes, *Transp. Porous Media* 96 (2) (2013) 221–235.
- [32] S. Porada, M. Bryjak, A. Van Der Wal, P. Biesheuvel, Effect of electrode thickness variation on operation of capacitive deionization, *Electrochim. Acta* 75 (2012) 148–156.
- [33] R. Zhao, M. Van Soestbergen, H. Rijnaarts, A. Van der Wal, M. Bazant, P. Biesheuvel, Time-dependent ion selectivity in capacitive charging of porous electrodes, *J. Colloid Interface Sci.* 384 (1) (2012) 38–44.
- [34] R. Zhao, P. Biesheuvel, A. Van der Wal, Energy consumption and constant current operation in membrane capacitive deionization, *Energ. Environ. Sci.* 5 (11) (2012) 9520–9527.
- [35] P. Biesheuvel, Y. Fu, M. Bazant, Electrochemistry and capacitive charging of porous electrodes in asymmetric multicomponent electrolytes, *Russ. J. Electrochem.* 48 (6) (2012) 580–592.
- [36] K. Laxman, M.T.Z. Myint, R. Khan, T. Pervez, J. Dutta, Effect of a semiconductor dielectric coating on the salt adsorption capacity of a porous electrode in a capacitive deionization cell, *Electrochim. Acta* 166 (2015) 329–337.
- [37] Y. Li, Y. Liu, J. Shen, J. Qi, J. Li, X. Sun, J. Shen, W. Han, L. Wang, Design of nitrogen-doped cluster-like porous carbons with hierarchical hollow nanoarchitecture and their enhanced performance in capacitive deionization, *Desalination* 430 (2018) 45–55.
- [38] Z. Chen, H. Zhang, C. Wu, L. Luo, C. Wang, S. Huang, H. Xu, A study of the effect of carbon characteristics on capacitive deionization (CDI) performance, *Desalination* 433 (2018) 68–74.
- [39] K. Laxman, L. Al Gharibi, J. Dutta, Capacitive deionization with asymmetric electrodes: Electrode capacitance vs electrode surface area, *Electrochim. Acta* 176 (2015) 420–425.
- [40] E.M. Remillard, A.N. Shocron, J. Rahill, M.E. Suss, C.D. Vecitis, A direct comparison of flow-by and flow-through capacitive deionization, *Desalination* 444 (2018) 169–177.
- [41] M.W. Saleem, W.-S. Kim, Parameter-based performance evaluation and optimization of a capacitive deionization desalination process, *Desalination* 437 (2018) 133–143.
- [42] H. Li, T. Lu, L. Pan, Y. Zhang, Z. Sun, Electrosorption behavior of graphene in NaCl solutions, *J. Mater. Chem.* 19 (37) (2009) 6773–6779.
- [43] P. Biesheuvel, S. Porada, M. Levi, M.Z. Bazant, Attractive forces in microporous carbon electrodes for capacitive deionization, *J. Solid State Electrochem.* 18 (5) (2014) 1365–1376.
- [44] J. Dykstra, R. Zhao, P. Biesheuvel, A. Van der Wal, Resistance identification and rational process design in capacitive deionization, *Water Res.* 88 (2016) 358–370.
- [45] J. Nordstrand, J. Dutta, Dynamic langmuir model: a simpler approach to modeling capacitive deionization, *J. Phys. Chem. C* 123 (26) (2019) 16479–16485.
- [46] J. Nordstrand, J. Dutta, Flexible modeling and control of capacitive-deionization processes through a linear-state-space dynamic Langmuir model, *npj Clean. Water* 4 (1) (2021) 1–7.
- [47] A. Hemmatifar, M. Stadermann, J.G. Santiago, Two-dimensional porous electrode model for capacitive deionization, *J. Phys. Chem. C* 119 (44) (2015) 24681–24694.
- [48] A. Usefian, M. Bayareh, Numerical and experimental investigation of an efficient convergent-divergent micromixer, *Meccanica* 55 (5) (2020) 1025–1035.
- [49] M.K. Parsa, F. Hormozi, D. Jafari, Mixing enhancement in a passive micromixer with convergent-divergent sinusoidal microchannels and different ratio of amplitude to wave length, *Comput. Fluids* 105 (2014) 82–90.
- [50] M. Lee, S. Jeong, S. Ahn, J. Han, Heat transfer and friction in rectangular convergent and divergent channels with ribs, *J. Thermophys. Heat Transfer* 27 (4) (2013) 660–667.
- [51] M. Nazari, S. Rashidi, J.A. Esfahani, Mixing process and mass transfer in a novel design of induced-charge electrokinetic micromixer with a conductive mixing-chamber, *Int. Commun. Heat Mass Transfer* 108 (2019) 104293.
- [52] A. Afzal, K.-Y. Kim, Convergent-divergent micromixer coupled with pulsatile flow, *Sens. Actuators B* 211 (2015) 198–205.
- [53] M.Z. Chowdhury, Y.E. Akansu, Novel convergent-divergent serpentine flow fields effect on PEM fuel cell performance, *Int. J. Hydrogen Energy* 42 (40) (2017) 25686–25694.
- [54] F. Heshmatnezhad, H. Aghaei, A.R.S. Nazar, Parametric study of obstacle geometry effect on mixing performance in a convergent-divergent micromixer with sinusoidal walls, *Chem. Prod. Process Model.* 12 (1) (2017).
- [55] L. Yang, S. Li, J. Liu, J. Cheng, Fluid mixing in droplet-based microfluidics with T junction and convergent-divergent sinusoidal microchannels, *Electrophoresis* 39 (3) (2018) 512–520.

- [56] R. Zhao, O. Satpradit, H. Rijnaarts, P. Biesheuvel, A. Van der Wal, Optimization of salt adsorption rate in membrane capacitive deionization, *Water Res.* 47 (5) (2013) 1941–1952.
- [57] H. Wang, L. Pilon, Accurate simulations of electric double layer capacitance of ultramicroelectrodes, *J. Phys. Chem. C* 115 (33) (2011) 16711–16719.
- [58] M.E. Suss, P. Biesheuvel, T.F. Baumann, M. Stadermann, J.G. Santiago, In situ spatially and temporally resolved measurements of salt concentration between charging porous electrodes for desalination by capacitive deionization, *Environ. Sci. Tech.* 48 (3) (2014) 2008–2015.
- [59] P.M. Biesheuvel, R. Zhao, S. Porada, A. Van der Wal, Theory of membrane capacitive deionization including the effect of the electrode pore space, *J. Colloid Interface Sci.* 360 (1) (2011) 239–248.
- [60] P. Biesheuvel, Y. Fu, M.Z. Bazant, Diffuse charge and Faradaic reactions in porous electrodes, *Phys. Rev. E* 83 (6) (2011) 061507.
- [61] H. Hadidi, R. Kamali, Numerical simulation of a non-equilibrium electrokinetic micro/nano fluidic mixer, *J. Micromech. Microeng.* 26 (3) (2016) 035019.
- [62] H. Hadidi, R. Kamali, M.K. Manshadi, Numerical simulation of a novel non-uniform electric field design to enhance the electrocoalescence of droplets, *Eur. J. Mech.-B/Fluids* 80 (2020) 206–215.
- [63] H. Hadidi, S.M. Mousavi, M. Ghalambaz, Numerical study of MHD natural heat transfer of non-Newtonian, carbon nanotube-water nanofluid inside an internally finned annulus, *Eur. Phys. J. Plus* 136 (9) (2021) 1–19.
- [64] J. Nordstrand, J. Dutta, A new automated model brings stability to finite-element simulations of capacitive deionization, *Nano Select* 3 (6) (2022) 1021–1035.
- [65] M. Bazmi, T. Tsotsis, K. Jessen, R. Ciora, D. Parsley, Advanced ceramic membranes/modules for ultra efficient hydrogen (H₂) production/carbon dioxide (CO₂) capture for coal-based polygeneration plants: fabrication, testing, and CFD modeling, Media and Process Technology Inc, 2022.
- [66] W. Xiaobing, L. Jinqiu, L. Yang, L. Sen, L. Dong, M. Tingting, J. An, H. Yanshe, G. Fengwei, Numerical analysis of capacitive deionization process using activated carbon electrodes, *Water Air Soil Pollut.* 232 (9) (2021) 1–10.
- [67] J. Bear, Dynamics of fluids in porous media, Courier Corporation, 1988.
- [68] M. Khosravikia, A. Rahbar-Kelishami, A simulation study of an applied approach to enhance drug recovery through electromembrane extraction, *J. Mol. Liq.* 358 (2022) 119210.
- [69] M. Khosravikia, Quantitative model for predicting the electroosmotic flow in Dual-Pole nanochannels, *Electrophoresis* (2023) 1–11.
- [70] P. Ratajczak, M.E. Suss, F. Kaasik, F. Béguin, Carbon electrodes for capacitive technologies, *Energy Storage Mater.* 16 (2019) 126–145.